Prediction of stability of tenfold-coordinated silica up to 200 TPa pressure based on *ab initio* calculations with all-electron pseudopotentials

Chuan Wang [1,2,3,*] Meng Lv,[1,2,3,*] Ronghao Hu [1,2,3,†] Junqing Wang [1,2,3,‡] and Yang Zhao[4]

[1]*College of Physics, Sichuan University, Chengdu 610065, People's Republic of China*

[2]*Key Laboratory of Radiation Physics and Technology, Ministry of Education, Chengdu 610064, People's Republic of China*

[3]*Key Laboratory of High Energy Density Physics and Technology, Ministry of Education, Chengdu 610064, People's Republic of China*

[4]*Research Center of Laser Fusion, China Academy of Engineering Physics, P. O. Box 919-986, Mianyang 621900, People's Republic of China*

(Received 1 January 2024; revised 13 March 2024; accepted 16 April 2024; published 26 April 2024)

The ultrahigh-pressure structural evolution and phase diagram of silica (SiO_2) from 10 TPa (10^{12} Pa) to 200 TPa are studied. Using a combination of *ab initio* simulations and a structure search algorithm, we reveal the phase diagram of SiO_2 above 10 TPa and confirm that $I4/mmm$ SiO_2 with the coordination number of 10 is the most stable phase of SiO_2 at ultrahigh pressures. The phase transition pressures from Fe_2P-type to $I4/mmm$ phase are obtained for different temperatures. To correctly model the ultrahigh-pressure structures, the inner-shell electron interactions are necessary to be considered. The pseudopotentials with different valence electron configurations are tested and the results show that neglecting the inner-shell electrons can predict incorrect phase transition sequence and thermodynamic stability. Based on simulations with all-electron pseudopotentials, it is found that the $I4/mmm$ SiO_2 is the most stable ten-coordinated structure up to 200 TPa. The thermodynamic stability of $I4/mmm$ SiO_2 up to a temperature of 8 kK is inferred from the Gibbs free energy calculations and the dynamic stability of $I4/mmm$ SiO_2 at 180 TPa is demonstrated by phonon calculations.

DOI: 10.1103/PhysRevB.109.134112

I. INTRODUCTION

Silica (SiO_2) is one of the key components of Earth, massive rocky planets and the rocky cores of gas giants. With the discovery of a great many terrestrial exoplanets, the high-pressure behavior of SiO_2 is of wide interest to geophysics, planetary and material sciences [1–9]. Super-Earths are usually rocky planets with masses of 1 to 10 times Earth's mass ($M_\oplus$), while much larger rocky planets with masses over 10 $M_\oplus$ are called mega-Earths. The mega-Earths discovered so far include K2-66b [10], Kepler-277c, and Kepler-277b [11], which have a mass of 21.3 $M_\oplus$, 64.2 $M_\oplus$, and 87.4 $M_\oplus$, respectively. The mantle layers of Kepler-277b and Kepler-277c are likely to contain $I4/mmm$ SiO_2 according to the equation of state (EOS) data and the mass-pressure relationship of SiO_2 [12]. High-pressure studies on SiO_2 and silicate (e.g., $MgSiO_3$ and $CaSiO_3$) show that SiO_2 undergoes a series of phase transitions: rutile-type → $CaCl_2$-type → α-PbO_2-type → pyrite (FeS_2)-type → Fe_2P-type phases at 48 GPa (10^9 Pa), 82 GPa, 190 GPa and 690 GPa respectively, with the coordination number (CoN) of Si increases to 9 [13–17]. And an cotunnite-type phase structurally intermediate between the Fe_2P-type and pyrite-type phases is found by theoretical calculation, suggesting possible temperature induced transformation [5]. The $R\bar{3}$ phase with the average CoN of 8 is also found theoretically, which fills the gaps of density and polyhedral occupancy between the pyrite-type and Fe_2P-type SiO_2 [18]. Experimentally, only phases up to pyrite-type SiO_2 have thus far been observed. In energy dispersive x-ray diffraction measurements on SiO_2 glass, the CoN of Si is observed to be greater than 6 [19,20], and changes in the x-ray absorption near edge structure with increasing density could be interpreted as an increase in the CoN of Si from 4 to 9 due to oxygen atoms [6]. Recent research on TiO_2 under high pressure theoretically predict the phase transition to $I4/mmm$ structure with CoN of 10 near 640 GPa. For SiO_2, an analogous phase transition occurs at 10 TPa (10^{12} Pa) [21].

The AX_2 compounds have similar high-pressure phase transition sequences. The nine-coordinated cotunnite-type structures for some oxides such as SiO_2, TiO_2, PbO_2 and CeO_2 have been synthesized [22–25]. The existence of stable ten-coordinated $I4/mmm$ structures for SiO_2, TiO_2, and CeO_2 has been predicted by theoretical calculations [21,26]. Eleven-coordinated Ni_2In-type structure has been experimentally observed for $PbCl_2$ and $BaCl_2$ [27,28]. For SiO_2, the existence of $I4/mmm$ to Ni_2In-type phase transition is yet to be explored. In experiments, SiO_2 has been compressed to less than 200 GPa [19,20]. For higher pressures, *ab initio* simulation is the most reliable tool to study the thermodynamic stability of SiO_2 [15,21]. In high-pressure studies of dioxide, the pseudopotentials of the two atoms is typically treated by considering the outermost electrons as valence electrons [3,18,29]. When the pressure is ultrahigh and atoms are very close to each other, the inner-shell electron interactions can no longer be neglected. Gao *et al.* constructed an all-electron pseudopotential for Si to study the equation of state and

*These authors contributed equally to this work.

†Corresponding author: ronghaohu@scu.edu.cn

‡Present address: Department of Engineering Physics, Tsinghua University, Beijing 100084, People's Republic of China.

principal Hugoniot at pressure up to 10^7 GPa, which agree well with experimental results [30]. Martinez-Canales *et al.* studied the phase transition sequence of carbon at pressures up to 1 PPa (10^{15} Pa), and they verified the reliability of their constructed all-electron ultrasoft pseudopotential for carbon by comparing with the results of the Coulomb potential [31].

In this paper, we investigate the thermodynamic stability of SiO_2 under pressures up to 200 TPa with *ab initio* simulations and the structure search method. The stabilities of the obtained phases at different temperatures are investigated and the structural phase diagram is obtained in the 10–200 TPa region with the quasi-harmonic free energy calculations. Pseudopotentials containing different numbers of valence electrons are constructed and tested. The all-electron pseudopotential is used for deep structure search of SiO_2 at 180 TPa. The Gibbs free energy calculations are performed to study the thermodynamic stability of SiO_2 with temperatures up to 8 kK, and phonon calculations are used to study the dynamic stability at 14.5 and 180 TPa.

II. COMPUTATIONAL METHOD

The thermodynamic stabilities of different crystalline structures are obtained by comparing their enthalpies under the static conditions within the framework of density functional theory (DFT). In order to confirm the most stable structure of SiO_2, a structure search method has been applied as an effective way to search the structure space. The phase diagram can be obtained by calculating and comparing the Gibbs free energies of different structures. And the dynamic stabilities are obtained by phonon calculations.

A. Density functional theory calculations

All simulations are performed based on the density functional molecular dynamics (DFT-MD) software Vienna *ab initio* simulation package (VASP) 5.4.4, as well as the QUANTUM ESPRESSO (QE) 7.2 package [32–34]. For the calculations of SiO_2, the $3s^23p^2$ (M shell), $2s^22p^63s^23p^2$ (L shell) and $1s^22s^22p^63s^23p^2$ (K shell) are chosen as valence electrons for Si, and the $2s^22p^4$ (L shell) and $1s^22s^22p^4$ (K shell) are chosen as valence electrons for O. The all-electron pseudopotential for Si and O in the projector augmented wave (PAW) format with a core radius (r_c) of both 0.5 bohr is generated using the ATOMPAW package [35]. The Vanderbilt scheme [36] is used to generate pseudo partial-waves $\tilde{\phi}_s^i(r)$ for each atomic type i, where an eighth-order polynomial function is used to pseudize the partial waves and is equal to the all-electron basis function $\phi_s^i(r)$ outside the atomic sphere. And it can be expressed as

$$\tilde{\phi}_s^i(r) = \begin{cases} r^{l_s+1}\sum_{m=0}^{4} C_m r^{2m} & \text{for } r < r_c \\ \phi_s^i(r) & \text{for } r \geqslant r_c, \end{cases} \tag{1}$$

where $s = (n_s,\ l_s,\ m_s)$ denotes the quantum state of the atom, and C_m is the coefficient of the polynomial of order $2m$. The Bessel scheme is used to get pseudopotential $\tilde{V}^i(r)$ from all-electron effective potential $V_{\text{eff}}^i(r)$ using a zero-order spherical Bessel function for $r < r_c$, and $\tilde{V}^i(r)$ is equal to $V_{\text{eff}}^i(r)$ for $r \geqslant r_c$, which can be expressed as

$$\tilde{V}^i(r) = \begin{cases} \alpha_0 \sin(q \cdot r)/r & \text{for } r < r_c \\ V_{\text{eff}}^i(r) & \text{for } r \geqslant r_c, \end{cases} \tag{2}$$

where α_0 is a parameter. The exchange-correlation energy is described using Perdew-Zunger (PZ) [37] parametrization of the local density approximation (LDA), Perdew-Burke-Ernzerhof (PBE) [38] and revised PBE for solid (PBEsol) [39] parametrization of the generalized gradient approximation (GGA), and Tao-Perdew-Staroverov-Scuseria (TPSS) [40] and strongly constrained and appropriately normed (SCAN) [41] parametrization of the meta-GGA. The detail settings for ion step convergence criterion, energy cutoff for the plane-wave basis, number of K points and number of bands for different calculation schemes can be found in Table I and all parameters have been tested to ensure the convergence of the enthalpy.

B. Crystalline structure search

The crystal structure search is implemented by crystal structure analysis by particle swarm optimization (CALYPSO) code based on particle swarm optimization algorithm within the evolutionary scheme [42–46], and structure relaxation is implemented by VASP an QE. A local PSO algorithm is used to avoid premature convergence, and during the crystal structure search, the number of formula units per cell is 3, 4, 5, 6, 7 for 10 and 15 TPa, and 2, 3, 4 for 150 and 180 TPa, respectively.

C. Thermodynamic property calculations and phonon calculations

We apply the finite displacement approach combined with the quasi-harmonic approximation (QHA) to determine the thermodynamic properties of these phases at finite temperatures. All calculations are implemented using the PHONOPY code [47]. When taking QHA into account, the Gibbs free energy is converted from Helmholtz energy as [15]

$$G(P, T) = F(V, T) + P(V, T)V, \tag{3}$$

where G and F are the Gibbs and Helmholtz free energies, P is pressure, V is volume and T is temperature. When the volume dependence of the thermal energy is represented within QHA, the Helmholtz free energy $F(V, T)$ can be written as [15]

$$F(V, T) = U_0(V) + \frac{1}{2}\sum_{q,i} h\omega_i(q, V) + k_B T \sum_{q,i} \ln\left[1 - \exp\left(-h\omega_i(q, V)/k_B T\right)\right], \tag{4}$$

where the three terms on the right-hand side of the above equation are the static lattice, zero-point and thermal contributions, respectively, and $\omega_i(q, V)$ is the frequency of the ith phonon mode at wave vector q. The phonon frequency ω_i is assumed to be independent of the temperature, which is valid when the temperature is not too high. The pressure $P(V, T)$ is calculated from the thermodynamic relation $P(V, T) = -[\partial F(V, T)/\partial V]_T$. The phonon dispersion relations are calculated based on the density functional perturbation theory

TABLE I. The parameter settings, computational platform and convergence of the enthalpy for SiO_2 with different valence electron configurations and pressure conditions are listed in the table. The parameters *a*, *b*, *c*, and *d* refer to ion step convergence criterion (in eV and Ry, where 1 Ry = 13.606 eV), energy cutoff of the plane wave basis (in eV and Ry), smallest allowed spacing between *K* points (in $Å^{-1}$), and number of bands, respectively.

Systems	Valence electron configuration	Pressure condition	*a*	*b*	*c*	*d*	Computing platform	Convergence of the enthalpy
SiO_2	Si: $3s^2 3p^2$ O: $2s^2 2p^4$ (*M-L*)	0.2–18 TPa	10^{-5} eV	850 eV	0.25	24	VASP	10^{-5} eV/atom
	Si: $3s^2 3p^2$ O: $2s^2 2p^4$ (*M-L*)	10–180 TPa	10^{-5} eV	1500 eV	0.25	21	VASP	10^{-3} eV/atom
	Si: $2s^2 2p^6 3s^2 3p^2$ O: $2s^2 2p^4$ (*L-L*)	10–180 TPa	10^{-5} eV	2000 eV	0.25	36	VASP	10^{-3} eV/atom
	Si: $2s^2 2p^6 3s^2 3p^2$ O: $1s^2 2s^2 2p^4$ (*L-K*)	10–180 TPa	10^{-5} eV	2000 eV	0.25	36	VASP	10^{-3} eV/atom
	Si: $1s^2 2s^2 2p^6 3s^2 3p^2$ O: $1s^2 2s^2 2p^4$ (*K-K*)	10–200 TPa	10^{-8} Ry	600 Ry	0.25	100	QE	10^{-3} Ry/atom

(DFPT) for 14.5 TPa and the finite displacement method for 180 TPa.

III. RESULTS AND DISCUSSION

A. Confirmation of the ten-coordinated structure of silicon dioxide

We carry out structure search for SiO_2 under 10 and 15 TPa, respectively. We find that the Fe_2P-type to $I4/mmm$ SiO_2 transition does not occur at 10 TPa. Although the enthalpy of the other structures is not competitive, it is still worth mentioning that the other silica structure with CoN = 10 (space group C_2/m) is found, as well as a mixed phase with the approximate characteristics of both Fe_2P-type and $I4/mmm$ structures. Then we confirm that $I4/mmm$ SiO_2 is the most stable structure under 15 TPa, that is, SiO_2 has changed from nine-coordinated structure to ten-coordinated structure under 15 TPa.

The calculated static enthalpy differences of several high-pressure structures of SiO_2 are demonstrated in Fig. 1 as a function of pressure. Below 1 TPa, a phase transition sequence from pyrite-type SiO_2 to Fe_2P-type is obtained, as plotted in Fig. 1(a). This indicates that the pressure induced transition occurs at about 0.67-0.68 TPa in the PBEsol calculation, which is 10–20 GPa lower than in the previous theoretical calculation [5,15], which is within an acceptable difference. Figure 1(b) portrays the Fe_2P-type to $I4/mmm$ SiO_2 phase transition sequence with GGA (PBE PBEsol) and LDA calculation. Using the PBEsol calculation, the enthalpy of Fe_2P-type SiO_2 is slightly higher than that of the $I4/mmm$ at about 14 TPa and there is a significant difference from the previous study [21], but consistent with results from simulations with inner-shell electron pseudopotentials, which can be found in Sec. III E. Our result indicates that Fe_2P-type SiO_2 is still more thermodynamically stable than $I4/mmm$ SiO_2 within the 10–14 TPa pressure range.

The phase transition sequence is also examined using PBE and LDA calculation. The transition pressure from Fe_2P-type to $I4/mmm$ is about 14.7 TPa by PBE calculation, 5% higher than the PBEsol calculation. LDA shifts the transition pressure of the post-Fe_2P-type phase to an obviously higher value: 15.6 TPa in the LDA calculation, 11% higher than in the PBEsol calculation. In this result, C_2/m SiO_2 possesses a lower enthalpy than Fe_2P-type SiO_2 at about 17.3 TPa. In our opinion, the reason for this difference between the PBEsol and LDA results is that, for the SiO_2 system, the uniformity of the charge density distribution varies greatly between Fe_2P-type and $I4/mmm$ SiO_2 at ultrahigh pressure [see Figs. 2(e) and 2(f)]. However, due to the outstanding performance in silica for other functionals [48], and due to the fact that the PBEsol functional is also sufficiently exact when considering the limit of a uniform electron gas, we tend to trust the result of the PBEsol calculation.

Static enthalpy consists of two different components, represented as E_{tot} and PV, where E_{tot} is the electronic total energy and PV represents the contributions of volume and pressure. To clarify the details of phase change, E_{tot} and PV are also demonstrated as functions of pressure in

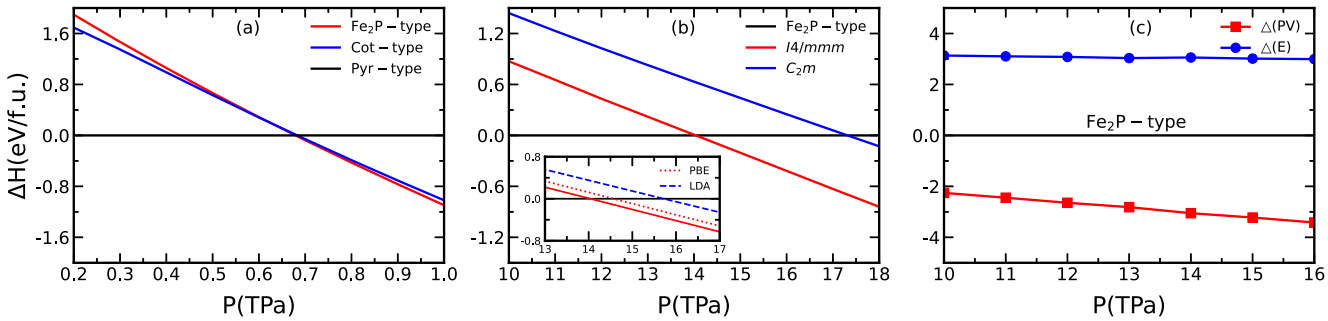

FIG. 1. (a) Static enthalpies of Fe_2P-type SiO_2 (red line) and Cot-type SiO_2 (blue line) with respect to the pyrite-type SiO_2 (horizontal black line), as calculated using GGA (PBEsol). The transition pressure is about 0.67–0.68 TPa, which is almost consistent with previous studies [5,15]. (b) The static enthalpies of $I4/mmm$ (red line) and C_2/m SiO_2 (blue line) with respect to Fe_2P-type SiO_2 are calculated using GGA (PBEsol), and the results of the LDA (blue dashed line) and PBE calculations (red dotted line) are plotted in (b) and the latter in the insert figure. (c) The pressure dependencies of $\bigtriangleup E_{tot}$ (blue dot line) and $\bigtriangleup (PV)$ (red dot line) between $I4/mmm$ and Fe_2P-type SiO_2.

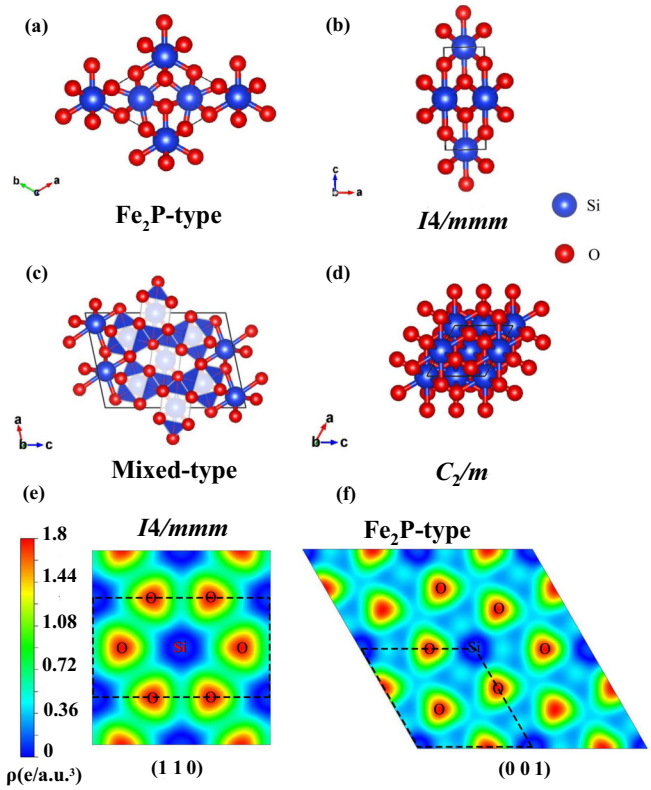

FIG. 2. Crystalline structures of (a) Fe_2P-type, (b) $I4/mmm$, (c) mixed-type, and (d) C_2/m SiO_2 at 14 TPa. The possible mixed structure has characteristics of both Fe_2P-type and $I4/mmm$, but the deformation is large. It contains two kinds of SiO_2 polyhedra with the CoNs of 9 and 10, which correspond to Fe_2P-type and $I4/mmm$ SiO_2, respectively. The charge densities are calculated using GGA (PBEsol) for (e) $I4/mmm$ SiO_2 on the (1 1 0) plane and for (f) Fe_2P-type SiO_2 on the (0 0 1) plane at 14 TPa. The unit cell is indicated by black dashed lines.

Fig. 1(c). The differences in these terms between Fe_2P-type and $I4/mmm$ SiO_2 show that $\triangle E_{tot}$ is almost constant while $\triangle (PV)$ decreases significantly with pressure, thereby indicating that the enthalpy crossover is mainly due to the volume contraction. In the case of pyrite-type to Fe_2P-type SiO_2, both the electronic total energy and the volume contraction contribute to the enthalpy crossover [15].

B. Ultrahigh-pressure crystalline structures of silica

The crystalline structures of Fe_2P-type, $I4/mmm$, the mixed-type and C_2/m SiO_2 at 14 TPa are demonstrated in Figs. 2(a)–2(d), respectively. The Fe_2P-type structure has a hexagonal lattice containing three nine-coordinated Si polyhedra with the space group $P\bar{6}2m$. The $I4/mmm$ structure has a tetragonal lattice that contains ten-coordinated Si polyhedra. The Si-O bond distances are 1.175–1.218 and 1.076–1.201 Å in $I4/mmm$ and Fe_2P-type SiO_2, respectively. Although the bond distance of $I4/mmm$ SiO_2 is shorter than that of Fe_2P-type, the polyhedral efficiency of the $I4/mmm$ is 0.855, which is higher than that of Fe_2P-type SiO_2 (about 0.79). The result of volume variation with pressure also indicates

TABLE II. Structural parameters of $I4/mmm$ and Fe_2P-type SiO_2 (as calculated with GGA (PBEsol) at 14 TPa) and of C_2/m and mixed-type SiO_2 at 10 TPa.

	$I4/mmm$ SiO_2	
Space group		$I4/mmm$
$(a,\ c)$		(1.431 Å 3.630 Å)
Si(1)	2b	(1/2 −1/2 0)
O(1)	4e	(1 −1 0.164)
	Fe_2P-type SiO_2	
Space group		$P\bar{6}2m$
$(a,\ c)$		(3.003 Å 1.441 Å)
Si(1)	2c	(1/3 2/3 1/2)
Si(2)	1b	(0 0 0)
O(1)	3f	(0.257 0 1/2)
O(2)	3g	(0.590 0 0)
	C_2m SiO_2	
Space group		C_2m
$(a\ b\ c)$		(2.151 Å 10.63 Å 2.161 Å)
$(\alpha\ \beta\ \gamma)$		(90° 61° 90°)
Si(1)	2b	(1/2 0 0)
Si(2)	4h	(1/2 0.3001 1/2)
Si(3)	4g	(1/2 0.3997 0)
O(1)	8j	(0.8290 0.4000 0.3297)
O(2)	4i	(0.8346 0 0.3259)
O(3)	8j	(0.6714 0.2001 0.1716)
	mixed-type SiO_2	
Space group		C_2m
$(a\ b\ c)$		(4.395 Å 1.595 Å 6.369 Å)
$(\alpha\ \beta\ \gamma)$		(90° 90° 90°)
Si(1)	2c	(1/2 1/2 1/2)
Si(2)	4i	(0.7421 0 0.2703)
Si(3)	4i	(0.8841 0 0.0585)
O(1)	4i	(0.9096 1/2 0.9135)
O(2)	4i	(0.0406 0 0.2529)
O(3)	4i	(0.6917 0 0.8443)
O(4)	4i	(0.6124 0 0.6306)
O(5)	4i	(0.1751 1/2 0.4378)

that the volume of $I4/mmm$ SiO_2 is always smaller than that of Fe_2P-type SiO_2 from 10 TPa to 18 TPa, and the volume contracts by 1.02% at the transition pressure. Hence, due to the higher coordination environment and smaller volume, the $I4/mmm$ SiO_2 is more stable than Fe_2P-type SiO_2. More details about the structures are presented in Table II.

The charge densities of Fe_2P-type and $I4/mmm$ SiO_2 under 14 TPa are also demonstrated in Figs. 2(e) and 2(f), respectively. In the $I4/mmm$ structure, the charge densities tend to concentrate upon O atoms. There is a large deformation due to ultrahigh pressure and charge densities are observed to be mostly triangular. In the Fe_2P-type structure, charge densities and Si atoms are both observed to be irregular, which could be a result of pressure further distorting the charge distribution.

C. Ultrahigh-pressure structure phase diagram of silica

The Gibbs free energies of Fe_2P-type and $I4/mmm$ SiO_2 are calculated using the QHA method. An ultrahigh P-T phase diagram is obtained by comparing the finite temperature

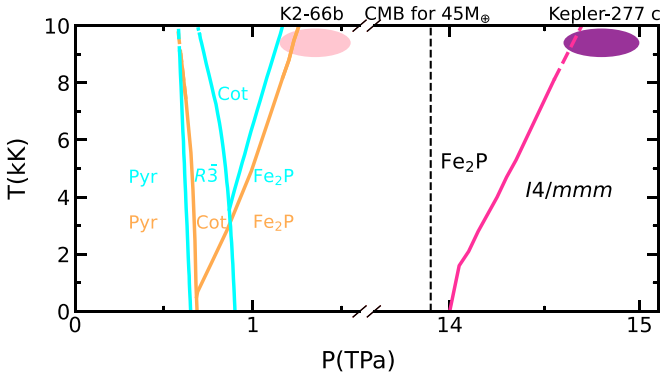

FIG. 3. An ultrahigh-pressure P-T diagram of SiO_2. Dashed boundaries indicate P, T conditions outside of the QHA validity range. The core-mantle boundary (CMB) pressures for a mega-Earth with 45 $M_\oplus$ are plotted by vertical dashed lines. The Gibbs free energies of pyrite-type, cotunnite-type, and Fe_2P-type SiO_2 marked in orange are from Ref. [15], and the Gibbs free energies of pyrite-type, $R\bar{3}$, cotunnite-type, and Fe_2P-type SiO_2 marked in cyan are from Ref. [18]. Additionally, the estimated and partial P, T ranges of mega-Earth's mantle are plotted. The pink and purple ellipses represent K2-66b [10], with more than 20 $M_\oplus$ and Kepler-277c with more than 60 $M_\oplus$, respectively.

Gibbs free energies of each phase. The result is shown in Fig. 3. The transition from pyrite-type SiO_2 to Fe_2P-type SiO_2 marked in orange is based upon the previous calculation [5,15]. The pyrite-type SiO_2 will directly transform to the Fe_2P-type SiO_2 at low temperature, while the cotunnite-type SiO_2 occurs between the pyrite- and Fe_2P-type SiO_2 at higher temperature. It also indicates that the cotunnite-type transitions to Fe_2P-type SiO_2 have a normal positive Clapeyron with strong temperature dependence. Similarly, the Fe_2P-type SiO_2 transform to $I4/mmm$ SiO_2 also has a strong positive temperature dependence. In addition, the phase $R\bar{3}$ with a mixed CoN has been found between pyrite- and Fe_2P-type phase, and the Gibbs free energies of pyrite-type, $R\bar{3}$, cotunnite-type and Fe_2P-type SiO_2 are marked in cyan. From the phase diagram we can see straight away that the exsitence of the $R\bar{3}$ phase does not significantly change the stable range of the pyrite-type phase, as well as the slop of the boundary line between the pyrite-type and post-pyrite-type phase, but significantly reduces the stable range of the cotunnite-type phase and increases the pressure at which the pure Fe_2P-type phase emerges [18]. In the transition from cotunnite-type to Fe_2P-type SiO_2, a mixed phase is founded and considered to be stable at high temperatures, leading not to a sharp transformation, but a gradual one [5]. In fact, a similar mixed phase between Fe_2P-type and $I4/mmm$ SiO_2 is also founded in the structure search process. The structure has characteristics of Fe_2P-type and $I4/mmm$ SiO_2, although the basic unit is deformed with lower symmetry. This may support the above view and explain the large temperature dependence. Moreover, since C_2/m SiO_2 is more stable than Fe_2P-type SiO_2 at about 17.3 TPa, it is also suspected to be a stable structure at a very high temperature.

According to the mass-pressure relationship of the terrestrial exoplanets, 13.9 TPa corresponds to the central pressure of a mega-Earth with about 45 times Earth's mass ($M_\oplus$) [12]. Fig. 3 also illustrates part of the P-T range of the mantle layers of K2-66b and Kepler-277c. K2-66b's lower mass suggests that $I4/mmm$ SiO_2 might not exit in it. At ultrahigh pressure, the $MgSiO_3$ and $CaSiO_3$ systems will finally dissociate into $MgO + SiO_2$ and $CaO + SiO_2$ and their phase diagrams will be determined similarly to SiO_2. Hence, the diagrams of $MgSiO_3$ and $CaSiO_3$ will be more abundant due to a study of the phase transition boundary of ten-coordinated SiO_2, which will contribute to the study of the massive terrestrial exoplanets' properties and mantle compositions. Additionally, $I4/mmm$ SiO_2 is metallized with compression induced band gap narrowing at about 1.4 TPa [21]. This suggests the possibility of studying the electrical conductivity or electromagnetic fields within a mega-Earth.

The dynamic stabilities of Fe_2P-type and $I4/mmm$ SiO_2 are also inspected by performing ab initio lattice-dynamics calculation on the basis of DFPT theory. The phonon dispersion under corresponding pressure is demonstrated in Fig. 4, indicating that both structures are dynamically stable. The maximum frequency of Fe_2P-type SiO_2 is higher

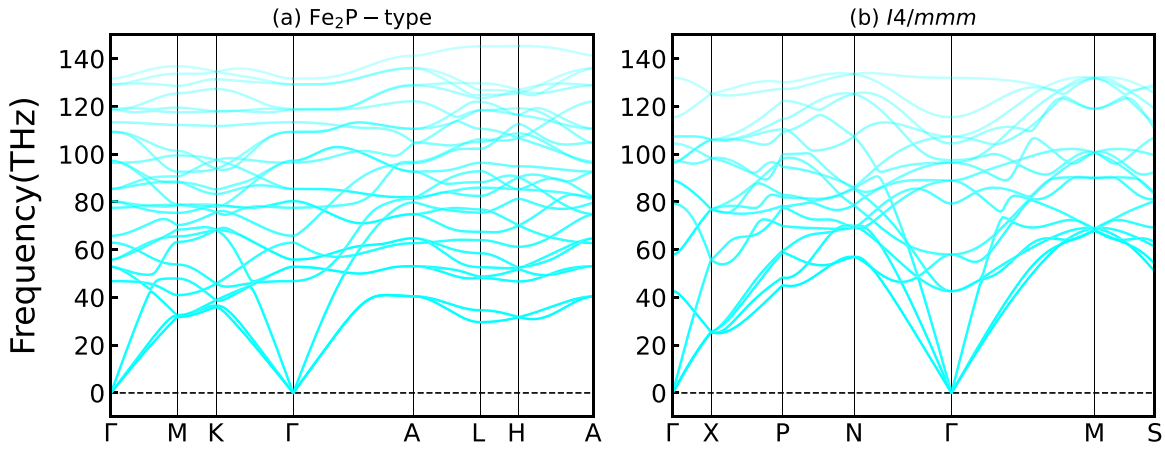

FIG. 4. Phonon-dispersion relations obtained by the PBEsol calculation. The results of (a) Fe_2P-type and (b) $I4/mmm$ SiO_2 at 14.5 TPa along the highly symmetric path.

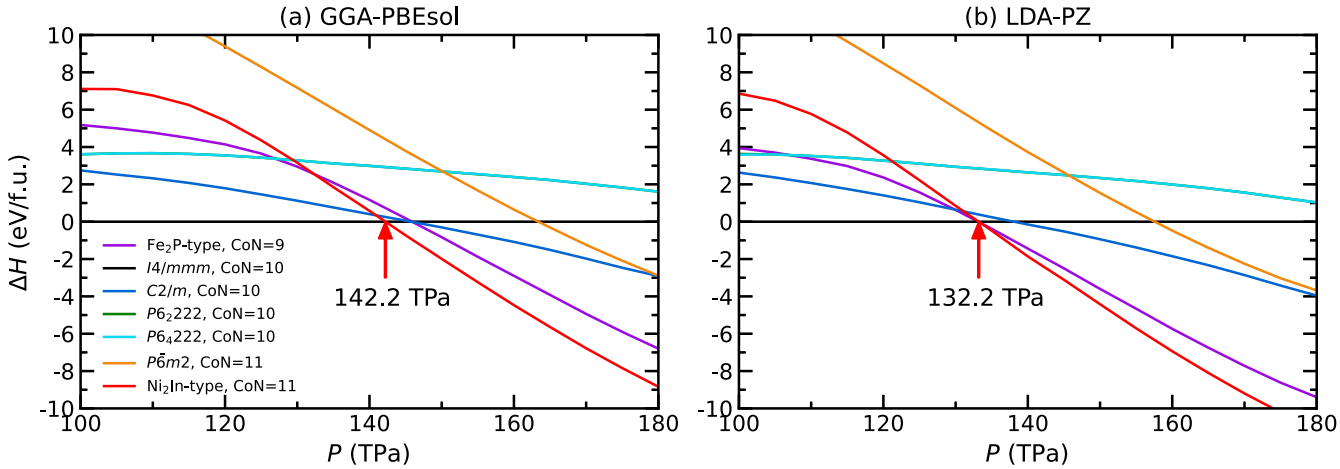

FIG. 5. The static enthalpies based on *M*-*L* pseudopotential with (a) GGA-PBEsol functional and (b) LDA-PZ functional of Fe_2P-type, $C2/m$, $P6_222$, $P6_422$, $P\bar{6}m2$ and Ni_2In-type SiO_2 differences relative to the $I4/mmm$ SiO_2 (horizontal black line) plotted as a function of pressure, where the $P6_222$ and $P6_422$ phases overlap in the figure because the enthalpies are almost identical. The calculated phase transition pressure from $I4/mmm$ phase to Ni_2In-type phase is indicated by the red arrow.

than 140 THz, while the maximum frequency of $I4/mmm$ is slightly lower than that of 140 THz. The phonon modes reflect the Si-O stretching motion, and the result indicates that the Si-O bond is a little stronger in Fe_2P-type SiO_2 than in $I4/mmm$ SiO_2.

D. Exploration of the eleven-coordinated structure of silicon dioxide with *M*-*L* pseudopotential

The phase transition sequence of AX_2 crystals suggests Ni_2In-type phase is the most probable eleven-coordinated structure of SiO_2, and the pressure at which this phase is stable is probably greater than 100 TPa. At this pressure, although more inner-shell electrons should be taken into account in the pseudopotentials, we first investigate the results of the pseudopotentials that consider the *M*-shell electrons of Si and the *L*-shell electrons of O as valence electrons (*M*-*L* pseudopotential) for the sake of simplicity. We perform the structural search for SiO_2 at 150 TPa based on GGA-PBEsol functionals and find Ni_2In-type phase to be the most stable structure at this pressure, and find several competitive phases. In Fig. 5, the static enthalpies of the phases of several competitive phase of SiO_2 found by the structure search differences relative to the $I4/mmm$ SiO_2 (ΔH) is plotted as a function of pressure. Both GGA-PBEsol and LDA-PZ functional support that Ni_2In-type SiO_2 is the most stable eleven-coordination phase, and the transition pressures from $I4/mmm$ to Ni_2In-type phase are 142.2 and 132.2 TPa, respectively.

The meta-GGA functional further takes into account the Laplacian of the density and kinetic energy density of the electrons on top of the GGA functional, and is believed to possess higher accuracy [40]. In order to check the influence of the exchange-correlation functional on the conclusions, we considered two meta-GGA functionals, TPSS and SCAN, and calculate the enthalpy versus pressure for the four phases of Fe_2P-type, $C2/m$, $I4/mmm$, and Ni_2In-type, and the results are shown in Fig. 6. All three functionals, GGA-PBEsol, meta-GGA-TPSS and meta-GGA-SCAN, support the phase transition process of SiO_2 from Fe_2P-type to $I4/mmm$ to Ni_2In-type with phase transition pressures of 14.0 and 142.2 TPa, 14.0 and 143.7 TPa, and 17.6 and 151.7 TPa, respectively. Moreover, the computational consumption of the meta-GGA functional is two to three times higher than that of the GGA functional, while the hybrid functional, which takes

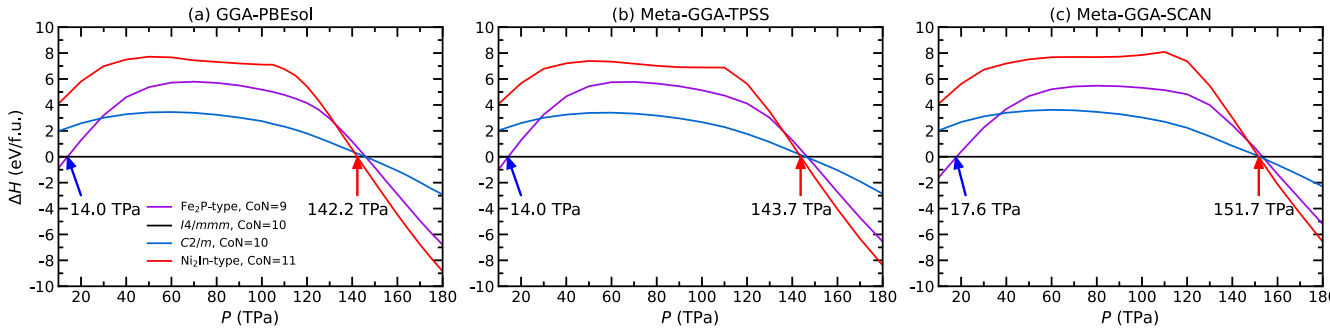

FIG. 6. The static enthalpies based on *M*-*L* pseudopotential with (a) GGA-PBEsol functional, (b) meta-GGA-TPSS functional and (c) meta-GGA-SCAN functional of Fe_2P-type, $C2/m$, and Ni_2In-type SiO_2 differences relative to the $I4/mmm$ SiO_2 (horizontal black line) plotted as a function of pressure. The calculated phase transition pressure from Fe_2P-type to $I4/mmm$ phase to Ni_2In-type phase is indicated by the blue and red arrows, respectively.

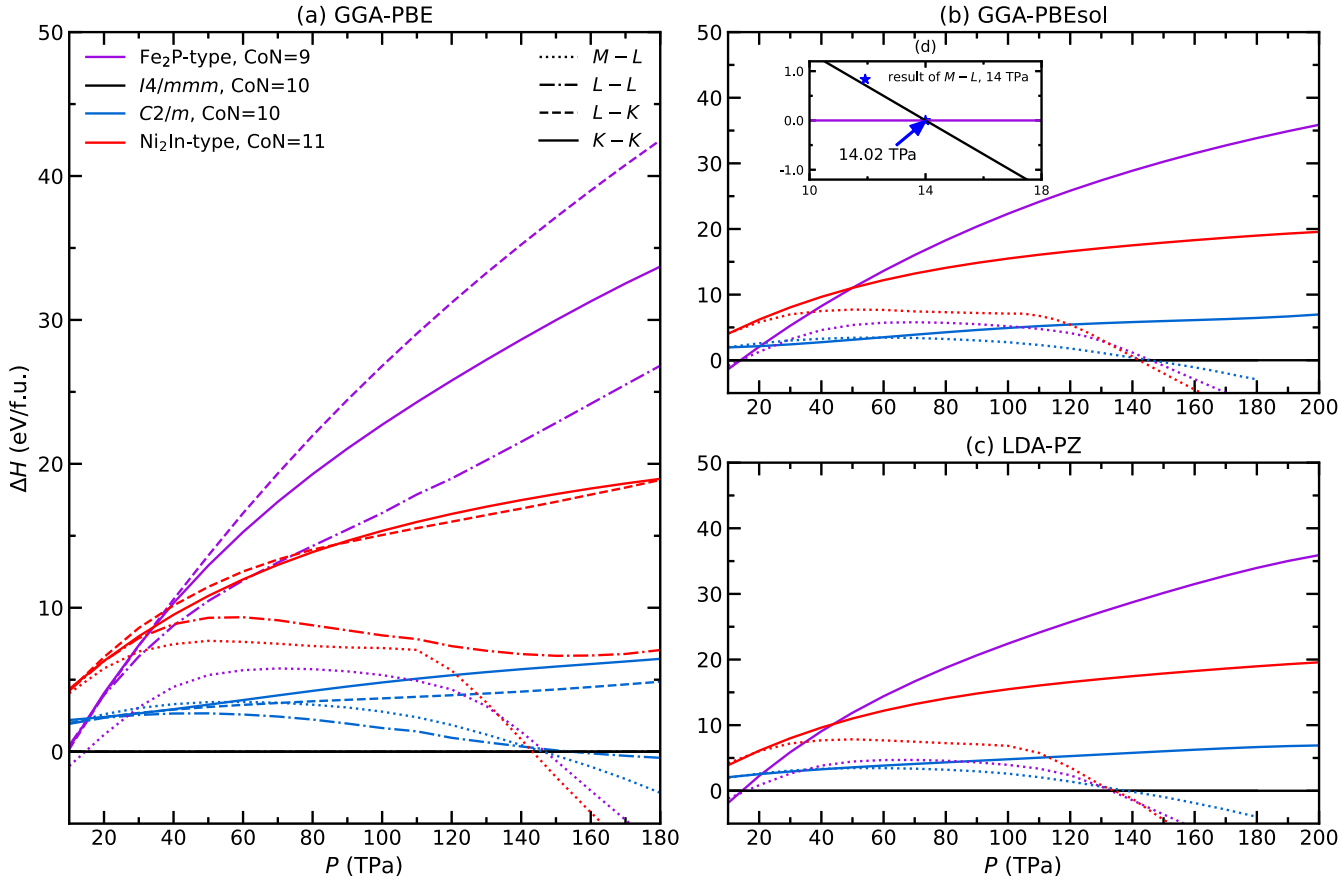

FIG. 7. The static enthalpies based on (a) GGA-PBE functional, (b) GGA-PBEsol functional and (c) LDA-PZ functional of Fe_2P-type, $C2/m$, and Ni_2In-type SiO_2 differences relative to the $I4/mmm$ SiO_2 (horizontal black line) plotted as a function of pressure. Dotted, dashdot, dashed and solid lines indicate the results of *M*-*L*, *L*-*L*, *L*-*K*, and *K*-*K* pseudopotentials, respectively. (d) The transition pressure from the Fe_2P-type phase to the $I4/mmm$ phase calculated by the *K*-*K* pseudopotential, while the result of the *M*-*L* pseudopotential is marked by blue pentagram.

into account the exact Hartree-Fock exchange energy, is four orders of magnitude higher than that of the GGA functional, which is beyond our computational capability.

E. The all-electron pseudopotentials

Although the above results support the phase transition of SiO_2 from $I4/mmm$ to Ni_2In-type phase, we should scrutinize the effect of the inner-shell electrons. For Si, we use the pseudopotentials considering *L*-shell and *K*-shell electrons as valence electrons, and for O, we use pseudopotentials considering *L*-shell and *K*-shell electrons as valence electrons. The results of the static enthalpies of Fe_2P-type, $C2/m$, and Ni_2In-type phases differences relative to the $I4/mmm$ SiO_2 based on the four pseudopotentials *M*-*L* (dotted line), *L*-*L* (dashdot line), *L*-*K* (dashed line), and *K*-*K* (solid line) with GGA-PBE functional is plotted as a function of pressure in Fig. 7(a). We observe very different results from the *M*-*L* pseudopotential. The results for the *L*-*L* pseudopotential show that the Fe_2P-type and Ni_2In-type phases are less stable than the $I4/mmm$ phase up to 180 TPa, while the $C2/m$ phase is observed to be more stable than the $I4/mmm$ phase near 154 TPa. However more precise results of *L*-*K* and *K*-*K* pseudopotentials support that the $I4/mmm$ phase is the most stable structure up to 180 TPa. The results of the *M*-*L* and *K*-*K* pseudopotential with the GGA-PBEsol and LDA-PZ functionals are shown in Figs. 7(b) and 7(c), respectively. And we can conclude that both the results of LDA-PZ, GGA-PBE and GGA-PBEsol functionals with *K*-*K* pseudopotentials support that the $I4/mmm$ SiO_2 is the most stable structure up to 200 TPa.

Figure 7(d) demonstrates that the transition pressure from the Fe_2P-type phase to the $I4/mmm$ phase calculated by the *K*-*K* pseudopotential is 14.02 TPa, which is almost the same as the result of the *M*-*L* pseudopotential of 14 TPa, which further proves the robustness of our constructed pseudopotential. In addition, in Fig. 7, we can further analyze the trend of enthalpy difference from different pseudopotentials. By comparing the results of the *M*-*L*, *L*-*L* and *L*-*K* pseudopotentials with the results of the *K*-*K* pseudopotential, we consider the pseudopotential to be valid at this pressure if the error is less than 15%. In the pressure range from 10.0 to 17.0 TPa, the accuracy of the *M*-*L* pseudopotential is acceptable. In the pressure range from 17.0 to 39.6 TPa, the results of *L*-*L*, *L*-*K*, and *K*-*K* pseudopotentials are almost the same, and it can be assumed that the *K*-shell electronic contributions of Si and O can be neglected. In the pressure range from 39.6 to 85.0 TPa, the *L*-*L* pseudopotential fails and the *K*-shell electronic

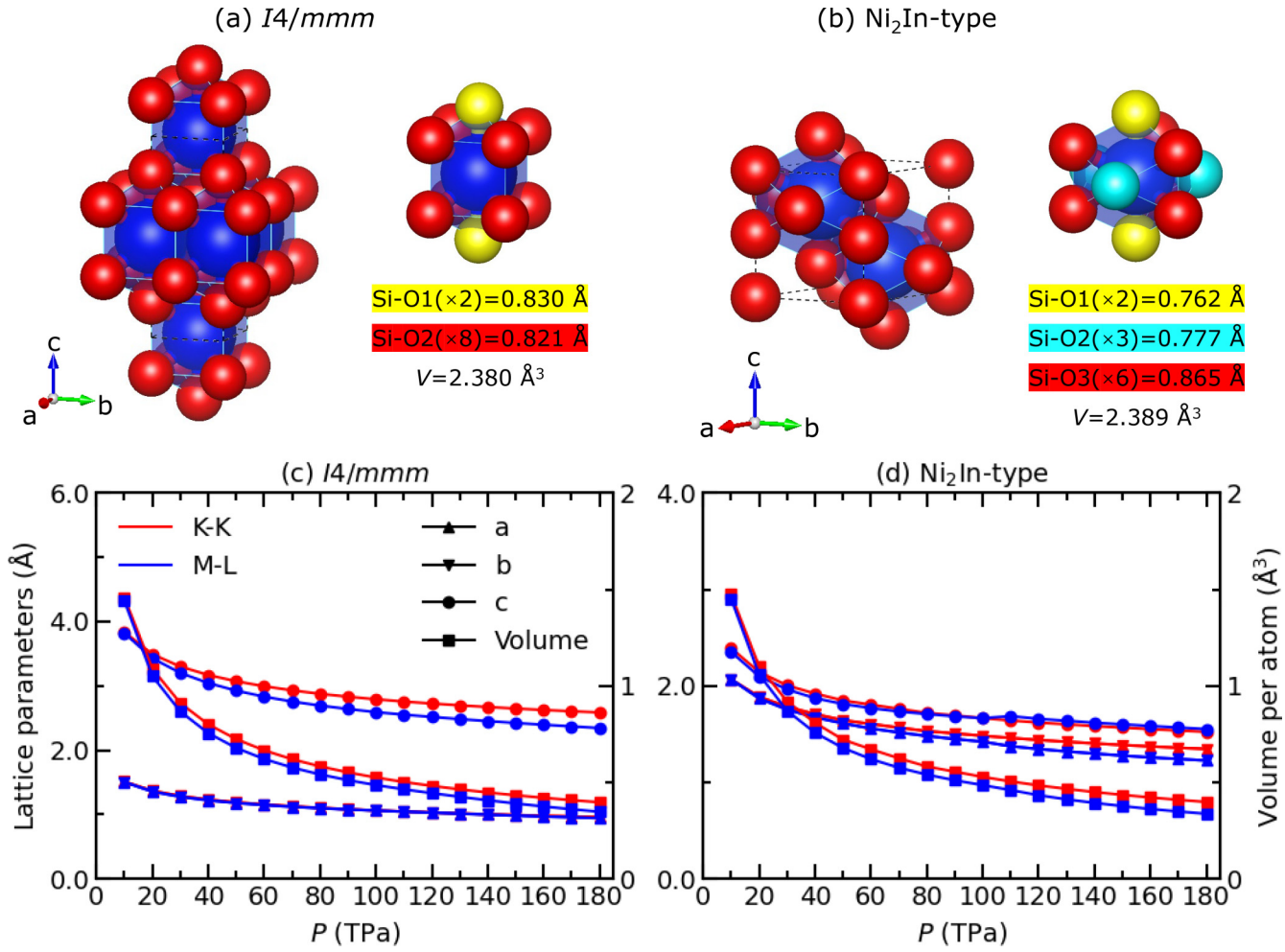

FIG. 8. Unit crystal structures of (a) $I4/mmm$ and (b) Ni_2In-type SiO_2 at 180 TPa. The lattice parameters for the $I4/mmm$ phase are $(a, b, c, \alpha, \beta, \gamma) = (0.96\,\text{Å}, 0.96\,\text{Å}, 2.59\,\text{Å}, 90^\circ, 90^\circ, 90^\circ)$, and for Ni_2In-type phase are $(a, b, c, \alpha, \beta, \gamma) = (1.34\,\text{Å}, 1.34\,\text{Å}, 1.52\,\text{Å}, 90^\circ, 90^\circ, 120^\circ)$. Si atoms are represented by the color blue, and the different O atoms are represented by the colors red, yellow and cyan, respectively. The crystal structure is rendered by VESTA [49]. The lattice parameters and volume for (c) $I4/mmm$ and (d) Ni_2In-type SiO_2 plotted as a function of pressure. The red and blue colors indicate the results of the K-K pseudopotential and the M-L pseudopotential, respectively. Lattice constants a, b, c, and the volume are indicated by upper triangular, lower triangular, circular and square dots, respectively.

contribution of O is not negligible. When the pressure is higher than 85.0 TPa, the K-shell electrons of Si need to be taken into account. A brief summary of the structural phase transitions predicted with different valence electron configurations and exchange-correlation functionals within 10–200 TPa and the effective pressure ranges of the pseudopotentials for different valence electron configurations can be found in Table III.

We perform the structural search for SiO_2 at 180 TPa to further confirm our conclusions. The results of the structural search are consistent with above calculations and support that the $I4/mmm$ phase is the most stable structure for SiO_2 up to 180 TPa. The unit crystal structures of $I4/mmm$ and Ni_2In-type SiO_2 at 180 TPa are shown in Figs. 8(a) and 8(b), respectively. $I4/mmm$ SiO_2 is a tetragonal structure in which the Si atoms are ten-coordinated, and the Si-O bond distances are 0.821–0.830 Å. Ni_2In-type (space group $P6_3/mmc$) SiO_2 is a hexagonal structure in which the Si atoms are eleven-coordinated, and the Si-O bond distances are 0.762–0.865 Å. The lattice parameters and volume versus pressure for $I4/mmm$ and Ni_2In-type SiO_2 are shown in Figs. 8(c) and 8(d), respectively. The results of the K-K pseudopotential show that the two phases have almost the same volume at 180 TPa, but the $I4/mmm$ phase has a lower energy. The erroneous conclusions of the M-L pseudopotential stem from the fact that the volume of Ni_2In-type phases compresses faster than that of the $I4/mmm$ phase, however, we can see from the Fig. 8(d), the result of the M-L pseudopotential at pressure greater than 110 TPa leads to a deformation of the cell (a and b decrease, c increases but keeps the volume almost the same), which suggests that the Ni_2In-type phase is no longer perfectly hexagonal, which is the direct evidence of the failure of the pseudopotential. Furthermore, the pressure of 180 TPa corresponds to the core pressure of massive super-Earth with the mass of more than 100 times the mass of the Earth [12], therefore $I4/mmm$ SiO_2 can be considered as the main component of its mantle layer.

TABLE III. The structural phase transitions predicted with different valence electron configurations and exchange-correlation functionals within 10–200 TPa. The effective pressure ranges of the pseudopotentials for different valence electron configurations are also listed in the table.

Valence electron configuration	Exchange-correlation functional	Structural phase transitions predicted within 10-200 TPa	Effective pressure range for pseudopotentials
M-L	LDA-PZ	Fe_2P-type $\xrightarrow{15.6\ TPa}$ $I4/mmm$ $\xrightarrow{132.2\ TPa}$ Ni_2In-type phase	10.0–17.0 TPa
	GGA-PBE	Fe_2P-type $\xrightarrow{14.7\ TPa}$ $I4/mmm$ $\xrightarrow{143.4\ TPa}$ Ni_2In-type phase	
	GGA-PBEsol	Fe_2P-type $\xrightarrow{14.0\ TPa}$ $I4/mmm$ $\xrightarrow{142.2\ TPa}$ Ni_2In-type phase	
	Meta-GGA-TPSS	Fe_2P-type $\xrightarrow{14.0\ TPa}$ $I4/mmm$ $\xrightarrow{143.7\ TPa}$ Ni_2In-type phase	
	Meta-GGA-SCAN	Fe_2P-type $\xrightarrow{17.6\ TPa}$ $I4/mmm$ $\xrightarrow{151.7\ TPa}$ Ni_2In-type phase	
L-L	GGA-PBE	Fe_2P-type $\xrightarrow{10.0\ TPa}$ $I4/mmm$ $\xrightarrow{153.4\ TPa}$ $C2/m$ phase	10.0–39.6 TPa
L-K	GGA-PBE	Fe_2P-type $\xrightarrow{10.0\ TPa}$ $I4/mmm$ phase	10.0–85.0 TPa
K-K	LDA-PZ	Fe_2P-type $\xrightarrow{14.6\ TPa}$ $I4/mmm$ phase	10.0–200.0 TPa
	GGA-PBE	Fe_2P-type $\xrightarrow{10.0\ TPa}$ $I4/mmm$ phase	
	GGA-PBEsol	Fe_2P-type $\xrightarrow{14.0\ TPa}$ $I4/mmm$ phase	

In order to explore the more stable structure at finite temperature, the Gibbs free energy at finite temperature needs to be considered. We calculated the Gibbs free energy based on *K-K* pseudopotential with GGA-PBEsol functional of Ni_2In-type SiO_2 differences relative to the $I4/mmm$ SiO_2 (ΔG) as a function of temperature at pressures ranging from 80 to 180 TPa, and the results are shown in Fig. 9. The results show that the $I4/mmm$ phase is more stable than the Ni_2In-type phase at pressures from 80 to 180 TPa and at temperatures from 0 to 8 kK. ΔG at 0 K increases with pressure, but the rate of increase gradually slows down, which is consistent with the static enthalpy results shown in Fig. 7. And ΔG decreases with increasing temperature, but only a slow decrease is observed up to 8 kK, suggesting that the Ni_2In-type phase at higher temperatures is a candidate for temperature-induced phase transitions, but this temperature is beyond the range of applicability of the QHA.

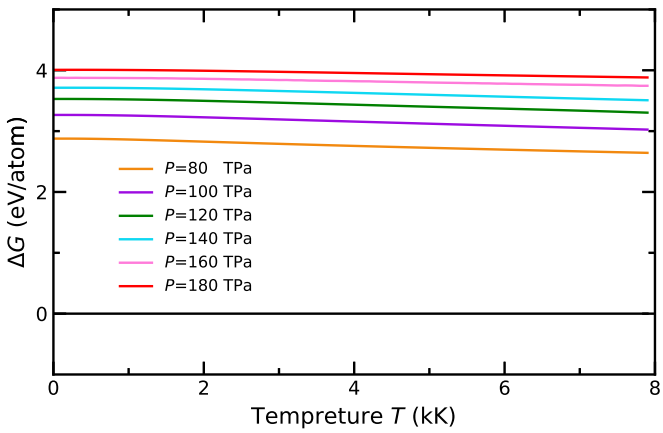

FIG. 9. The Gibbs free energy based on *K-K* pseudopotential with GGA-PBEsol functional of Ni_2In-type SiO_2 differences relative to the $I4/mmm$ SiO_2 (horizontal black line) plotted as a function of temperature at pressures ranging from 80 to 180 TPa.

The calculated phonon dispersion and projected density of states (PDOS) curves of the $I4/mmm$ phase at 180 TPa based on *K-K* pseudopotential with GGA-PBEsol functional are shown in Fig. 10. The results show that there is no imaginary mode in $I4/mmm$ phase at 180 TPa, which proves the robust dynamic stability of $I4/mmm$ phase. The PDOS results show a comparable contribution from the motion of Si and O atoms in the lower-frequency region (0–175 THz) and a more significant contribution from the motion of O atoms in the upper-frequency region (175–345 THz). The calculated band gap and phonon zero-point energy (ZPE) of pyrite-type, Fe_2P-type and $I4/mmm$ SiO_2 with GGA-PBEsol functional as a function of pressure are shown in Figs. 11(a) and 11(b), respectively. And our results are consistent with those of Ref. [16] below 3 TPa. Figure 11(a) show that the band gap

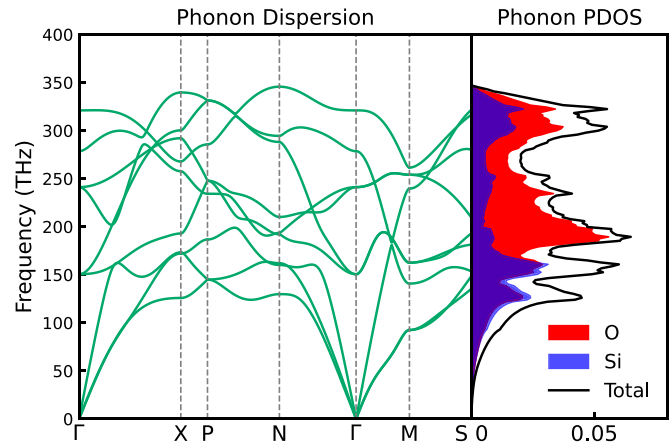

FIG. 10. Phonon-dispersion relations (left) and PDOS curves (right) of the $I4/mmm$ phase at 180 TPa based on *K-K* pseudopotential with GGA-PBEsol functional. In the PDOS plot, the projections onto Si and O atoms are shown as overlaid blue and Red shaded curves, and the total phonon density of states is represented by the black curve.

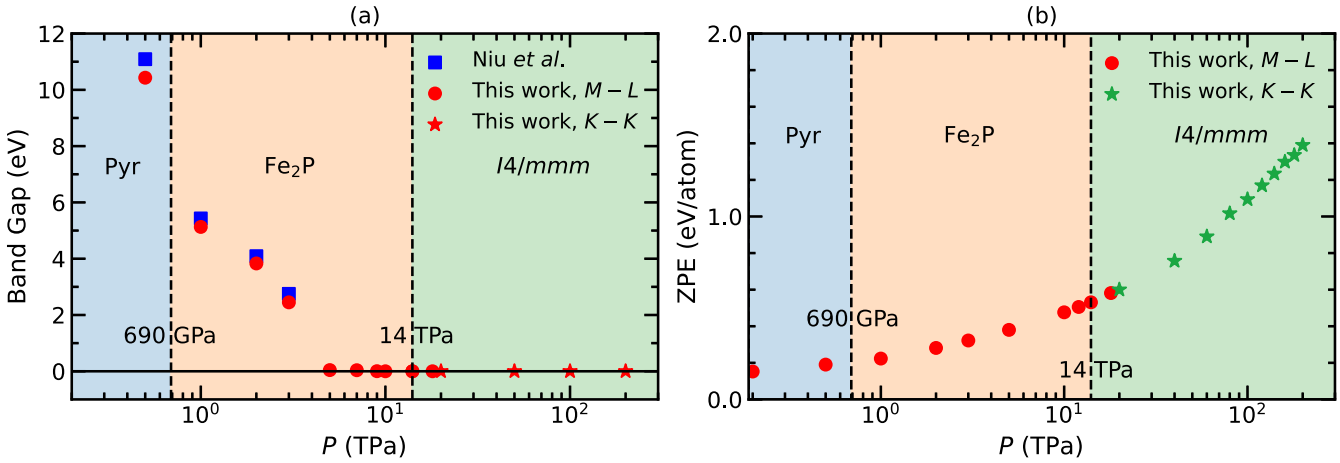

FIG. 11. Calculated (a) band gap and (b) ZPE of pyrite-type, Fe_2P-type and $I4/mmm$ SiO_2 with GGA-PBEsol functional as a function of pressure. The band gaps and ZPE for 0.5–18 TPa is calculated by *M*-*L* pseudopotential, and the band gaps and ZPE for 20–200 TPa is calculated by *K*-*K* pseudopotential. The band gaps for 0.5–3 TPa marked by blue squares are from Ref. [16].

of Fe_2P-type SiO_2 becomes 0 at about 10 TPa, indicating that SiO_2 becomes a metal at about 10 TPa, and $I4/mmm$ SiO_2 is metallic at 14–200 TPa. The ZPE characterizes the vibrational contribution to the free energy at 0 K. The calculated ZPE increases with the increasing pressure, as shown in Fig. 11(b). The increased ZPE under ultrahigh pressures comes from the contributions due to overlap of electron shells of neighboring atoms and deformation of electron shells.

IV. CONCLUSION

Structure searches of SiO_2 based on *ab initio* simulations are performed to systematically explore the structure space of SiO_2 at 10 TPa and 15 TPa. At 10 TPa, the Fe_2P-type structure is the most stable form of SiO_2 with CoN=9, and at 15 TPa, SiO_2 has changed from nine-coordinated structure to ten-coordinated structure ($I4/mmm$ structure). The enthalpies of Fe_2P-type and $I4/mmm$ structures show that the phase transition pressure at 0 K is about 14 TPa. The phase transition pressure increases with the temperature. The structure phase space with pressure range from 10 to 15 TPa and temperature range from 0 to 10 kK is obtained from the calculated Gibbs free energies of Fe_2P-type and $I4/mmm$ SiO_2. No temperature induced transitions are found in this *P*-*T* range. The ultrahigh-pressure structural stability and phase diagram of SiO_2 are essential for understanding the structure and property of the planetary core of super-massive planets like Kepler-277b and Kepler-277c. The results show that $I4/mmm$ SiO_2 are possibly inside the mantle of a mega-Earth with a mass of about 45 $M_\oplus$. A richer SiO_2 phase diagram under ultrahigh pressure also provides a new reference for the phase diagrams of $MgSiO_3$ and $CaSiO_3$. The $I4/mmm$ structures in TiO_2 and SiO_2 also provide a reference for possible high-pressure structures of other AX_2 compounds.

And then the structure and thermodynamic stability of SiO_2 at pressures up to 200 TPa are investigated with *ab initio* simulations. The pseudopotentials containing different numbers of valence electrons are constructed and tested. The pseudopotentials considering only the outermost electrons can predict incorrect phase transition sequence and thermodynamic stability at ultrahigh pressures. For SiO_2, the *M*-*L*s, pseudopotential predicts the incorrect $I4/mmm$ to Ni_2In-type phase transitions at about 140 TPa. It is found that the all-electron *K*-*K* pseudopotential is the most reliable pseudopotential for SiO_2 at pressures above 20 TPa. With the all-electron pseudopotential, we confirm that $I4/mmm$ SiO_2 is the most stable phase up to 200 TPa by structure search, Gibbs free energy calculations and phonon calculations. Our results reveal the importance of all-electron pseudopotentials in ultrahigh-pressure simulations. The proposed methods can be used in the ultrahigh-pressure studies of other materials, such as TiO_2, CeO_2, and PbO_2.

ACKNOWLEDGMENTS

This work was partially supported by the National Natural Science Foundation of China under Grant No. 12374261.

[1] L. S. Dubrovinsky, S. K. Saxena, P. Lazor, R. Ahuja, O. Eriksson, J. M. Wills, and B. Johansson, Experimental and theoretical identification of a new high-pressure phase of silica, Nature (London) **388**, 362 (1997).

[2] S. Ono, K. Hirose, M. Murakami, and M. Isshiki, Post-stishovite phase boundary in SiO_2 determined by in situ X-ray observations, Earth Planet. Sci. Lett. **197**, 187 (2002).

[3] A. R. Oganov, M. J. Gillan, and G. D. Price, Structural stability of silica at high pressures and temperatures, Phys. Rev. B **71**, 064104 (2005).

[4] Y. Kuwayama, K. Hirose, N. Sata, and Y. Ohishi, The pyrite-type high-pressure form of silica, Science **309**, 923 (2005).

[5] S. Wu, K. Umemoto, M. Ji, C.-Z. Wang, K.-M. Ho, and R. M. Wentzcovitch, Identification of post-pyrite phase transitions in SiO_2 by a genetic algorithm, Phys. Rev. B **83**, 184102 (2011).

[6] A. Denoeud, S. Mazevet, F. Guyot, F. Dorchies, J. Gaudin, A. Ravasio, E. Brambrink, and A. Benuzzi-Mounaix, High-pressure structural changes in liquid silica, Phys. Rev. E **94**, 031201(R) (2016).

[7] M. Millot, N. Dubrovinskaia, A. Černok, S. Blaha, L. Dubrovinsky, D. G. Braun, P. M. Celliers, G. W. Collins, J. H. Eggert, and R. Jeanloz, Shock compression of stishovite and melting of silica at planetary interior conditions, Science **347**, 418 (2015).

[8] S. Zhang, M. A. Morales, R. Jeanloz, M. Millot, S. X. Hu, and E. Zurek, Nature of the bonded-to-atomic transition in liquid silica to TPa pressures, J. Appl. Phys. **131**, 071101 (2022).

[9] K. P. Driver, R. E. Cohen, Z. Wu, B. Militzer, P. L. Ríos, M. D. Towler, R. J. Needs, and J. W. Wilkins, Quantum Monte Carlo computations of phase stability, equations of state, and elasticity of high-pressure silica, Proc. Natl. Acad. Sci. USA **107**, 9519 (2010).

[10] P. Futó, Kepler-145b and K2-66b: A Kepler- and a K2-Mega-Earth with Different Compositional Characteristics, in Lunar and Planetary Science Conference, *Lunar and Planetary Science Conference* (Lunar and Planetary Institute, Houston, Texas, 2018), p. 1224.

[11] P. Futó, Kepler-277 b: A Supermassive Terrestrial Exoplanet in the Kepler-277 Planetary System, in *Lunar and Planetary Science Conference, Lunar and Planetary Science Conference* (Lunar and Planetary Institute, Houston, Texas, 2020), p. 1055.

[12] D. C. Swift, J. H. Eggert, D. G. Hicks, S. Hamel, K. Caspersen, E. Schwegler, G. W. Collins, N. Nettelmann, and G. J. Ackland, Mass–radius relationships for exoplanets, Astrophys. J. **744**, 59 (2012).

[13] K. Umemoto, R. M. Wentzcovitch, and P. B. Allen, Dissociation of $MgSiO_3$ in the cores of gas giants and terrestrial exoplanets, Science **311**, 983 (2006).

[14] K. Umemoto and R. M. Wentzcovitch, Two-stage dissociation in $MgSiO_3$ post-perovskite, Earth Planet. Sci. Lett. **311**, 225 (2011).

[15] T. Tsuchiya and J. Tsuchiya, Prediction of a hexagonal SiO_2 phase affecting stabilities of $MgSiO_3$ and $CaSiO_3$ at multi-megabar pressures, Proc. Natl. Acad. Sci. USA **108**, 1252 (2011).

[16] H. Niu, A. R. Oganov, X.-Q. Chen, and D. Li, Prediction of novel stable compounds in the Mg-Si-O system under exoplanet pressures, Sci. Rep. **5**, 18347 (2015).

[17] K. Umemoto, R. M. Wentzcovitch, S. Wu, M. Ji, C.-Z. Wang, and K.-M. Ho, Phase transitions in $MgSiO_3$ post-perovskite in super-Earth mantles, Earth Planet. Sci. Lett. **478**, 40 (2017).

[18] C. Liu, J. Shi, H. Gao, J. Wang, Y. Han, X. Lu, H.-T. Wang, D. Xing, and J. Sun, Mixed coordination silica at megabar pressure, Phys. Rev. Lett. **126**, 035701 (2021).

[19] C. Prescher, V. B. Prakapenka, J. Stefanski, S. Jahn, L. B. Skinner, and Y. Wang, Beyond sixfold coordinated Si in SiO_2 glass at ultrahigh pressures, Proc. Natl. Acad. Sci. USA **114**, 10041 (2017).

[20] Y. Kono, Y. Shu, C. Kenney-Benson, Y. Wang, and G. Shen, Structural evolution of SiO_2 glass with Si coordination number greater than 6, Phys. Rev. Lett. **125**, 205701 (2020).

[21] M. J. Lyle, C. J. Pickard, and R. J. Needs, Prediction of 10-fold coordinated TiO_2 and SiO_2 structures at multimegabar pressures, Proc. Natl. Acad. Sci. USA **112**, 6898 (2015).

[22] L. S. Dubrovinsky, N. A. Dubrovinskaia, V. Swamy, J. Muscat, N. M. Harrison, R. Ahuja, B. Holm, and B. Johansson, The hardest known oxide, Nature (London) **410**, 653 (2001).

[23] N. A. Dubrovinskaia, L. S. Dubrovinsky, R. Ahuja, V. B. Prokopenko, V. Dmitriev, H.-P. Weber, J. M. Osorio-Guillen, and B. Johansson, Experimental and theoretical identification of a new high-pressure TiO_2 polymorph, Phys. Rev. Lett. **87**, 275501 (2001).

[24] J. Haines, J. M. Léger, and O. Schulte, The high-pressure phase transition sequence from the rutile-type through to the cotunnite-type structure in PbO_2, J. Phys.: Condens. Matter **8**, 1631 (1996).

[25] S. J. Duclos, Y. K. Vohra, A. L. Ruoff, A. Jayaraman, and G. P. Espinosa, High-pressure x-ray diffraction study of CeO_2 to 70 GPa and pressure-induced phase transformation from the fluorite structure, Phys. Rev. B **38**, 7755 (1988).

[26] H. X. Song, L. Liu, H. Y. Geng, and Q. Wu, First-principle study on structural and electronic properties of CeO_2 and ThO_2 under high pressures, Phys. Rev. B **87**, 184103 (2013).

[27] S. M. Dorfman, F. Jiang, Z. Mao, A. Kubo, Y. Meng, V. B. Prakapenka, and T. S. Duffy, Phase transitions and equations of state of alkaline earth fluorides CaF_2, SrF_2, and BaF_2 to Mbar pressures, Phys. Rev. B **81**, 174121 (2010).

[28] T. J. Smart, E. F. O'Bannon, M. R. Diamond, S. Stackhouse, B. K. Godwal, Q. Williams, and R. Jeanloz, Equation of state, phase transitions, and band-gap closure in $PbCl_2$ and $SnCl_2$, Phys. Rev. B **107**, 134113 (2023).

[29] S. Ding, P. Zhang, K. Yang, C. Liu, J. Hao, W. Cui, J. Shi, and Y. Li, Formation of solid SiO_2He compound at high pressure and high temperature, Phys. Rev. B **106**, 024102 (2022).

[30] C. Gao, X. Liu, S. Zhang, W. Kang, P. Zhang, and X. T. He, Consistent wide-range equation of state of silicon by a unified first-principles method, Phys. Rev. B **107**, 165150 (2023).

[31] M. Martinez-Canales, C. J. Pickard, and R. J. Needs, Thermodynamically stable phases of carbon at multiterapascal pressures, Phys. Rev. Lett. **108**, 045704 (2012).

[32] G. Kresse and J. Hafner, Ab initio molecular dynamics for liquid metals, Phys. Rev. B **47**, 558 (1993).

[33] G. Kresse and J. Furthmüller, Efficient iterative schemes for ab initio total-energy calculations using a plane-wave basis set, Phys. Rev. B **54**, 11169 (1996).

[34] P. Giannozzi, S. Baroni, N. Bonini, M. Calandra, R. Car, C. Cavazzoni, D. Ceresoli, G. L. Chiarotti, M. Cococcioni, I. Dabo, A. D. Corso, S. de Gironcoli, S. Fabris, G. Fratesi, R. Gebauer, U. Gerstmann, C. Gougoussis, A. Kokalj, M. Lazzeri, L. Martin-Samos *et al.*, QUANTUM ESPRESSO: A modular and open-source software project for quantum simulations of materials, J. Phys.: Condens. Matter **21**, 395502 (2009).

[35] N. Holzwarth, A. Tackett, and G. Matthews, A Projector Augmented Wave (PAW) code for electronic structure calculations, Part I: *atompaw* for generating atom-centered functions, Comput. Phys. Commun. **135**, 329 (2001).

[36] D. Vanderbilt, Soft self-consistent pseudopotentials in a generalized eigenvalue formalism, Phys. Rev. B **41**, 7892 (1990).

[37] D. M. Ceperley and B. J. Alder, Ground state of the electron gas by a stochastic method, Phys. Rev. Lett. **45**, 566 (1980).

[38] J. P. Perdew, K. Burke, and M. Ernzerhof, Generalized gradient approximation made simple, Phys. Rev. Lett. **77**, 3865 (1996).

[39] J. P. Perdew, A. Ruzsinszky, G. I. Csonka, O. A. Vydrov, G. E. Scuseria, L. A. Constantin, X. Zhou, and K. Burke, Restoring

the density-gradient expansion for exchange in solids and surfaces, Phys. Rev. Lett. **100**, 136406 (2008).

[40] J. Sun, M. Marsman, G. I. Csonka, A. Ruzsinszky, P. Hao, Y.-S. Kim, G. Kresse, and J. P. Perdew, Self-consistent meta-generalized gradient approximation within the projector-augmented-wave method, Phys. Rev. B **84**, 035117 (2011).

[41] J. Sun, A. Ruzsinszky, and J. P. Perdew, Strongly constrained and appropriately normed semilocal density functional, Phys. Rev. Lett. **115**, 036402 (2015).

[42] Y. Wang, J. Lv, L. Zhu, and Y. Ma, Crystal structure prediction via particle-swarm optimization, Phys. Rev. B **82**, 094116 (2010).

[43] Y. Wang, J. Lv, L. Zhu, and Y. Ma, CALYPSO: A method for crystal structure prediction, Comput. Phys. Commun. **183**, 2063 (2012).

[44] B. Gao, P. Gao, S. Lu, J. Lv, Y. Wang, and Y. Ma, Interface structure prediction via CALYPSO method, Sci. Bull. **64**, 301 (2019).

[45] A. R. Oganov, J. Chen, C. Gatti, Y. Ma, Y. Ma, C. W. Glass, Z. Liu, T. Yu, O. O. Kurakevych, and V. L. Solozhenko, Ionic high-pressure form of elemental boron, Nature (London) **457**, 863 (2009).

[46] H. Dekura, T. Tsuchiya, Y. Kuwayama, and J. Tsuchiya, Theoretical and experimental evidence for a new post-cotunnite phase of titanium dioxide with significant optical absorption, Phys. Rev. Lett. **107**, 045701 (2011).

[47] A. Togo and I. Tanaka, First principles phonon calculations in materials science, Scr. Mater. **108**, 1 (2015).

[48] L. He, F. Liu, G. Hautier, M. J. T. Oliveira, M. A. L. Marques, F. D. Vila, J. J. Rehr, G.-M. Rignanese, and A. Zhou, Accuracy of generalized gradient approximation functionals for density-functional perturbation theory calculations, Phys. Rev. B **89**, 064305 (2014).

[49] K. Momma and F. Izumi, *VESTA3* for three-dimensional visualization of crystal, volumetric and morphology data, J. Appl. Crystallogr. **44**, 1272 (2011).